

Self-driving lab discovers principles for steering spontaneous emission

Saaketh Desai, Sadhvikas Addamane, Jeffery Y. Tsao, Igal Brener, Remi Dingreville, Prasad P. Iyer*

Center for Integrated Nanotechnologies, Sandia National Lab, Albuquerque NM, USA

ppadma@sandia.gov

Abstract

We develop an autonomous experimentation platform to accelerate interpretable scientific discovery in ultrafast nanophotonics, targeting a novel method to steer spontaneous emission from reconfigurable semiconductor metasurfaces. Controlling spontaneous emission is crucial for clean-energy solutions in illumination, thermal radiation engineering, and remote sensing. Despite the potential of reconfigurable semiconductor metasurfaces with embedded sources for spatiotemporal control, achieving arbitrary far-field control remains challenging. Here, we present a self-driving lab (SDL) platform that addresses this challenge by discovering the governing equations for predicting the far-field emission profile from light-emitting metasurfaces. We discover that both the spatial gradient (grating-like) and the curvature (lens-like) of the local refractive index are key factors in steering spontaneous emission. The SDL employs a machine-learning framework comprising: (1) a variational autoencoder for generating complex spatial refractive index profiles, (2) an active learning agent for guiding experiments with real-time closed-loop feedback, and (3) a neural network-based equation learner to uncover structure-property relationships. The SDL demonstrates a four-fold enhancement in peak emission directivity (up to 77%) over a 72° field of view within ~ 300 experiments. Our findings reveal that combinations of positive gratings and lenses are as effective as negative lenses and gratings for all emission angles, offering a novel strategy for controlling spontaneous emission beyond conventional Fourier optics.

Introduction

Self-driving labs (SDLs) represent a transformative approach to scientific discovery, employing machine-learning (ML) models to autonomously conduct experiments¹⁻¹⁰. Current experiments within SDLs focus on low-dimensional problems due to the challenges in interpreting high dimensional ($>10^3$ degrees of freedom) data structures¹¹⁻¹⁸. Hence, SDLs have primarily concentrated on optimization tasks within low-dimensional or well-understood search spaces, accelerating discovery in material science and chemistry¹⁹⁻²⁶. However, realizing interpretable scientific discovery²⁷ for high-dimensional problems presents a significant challenge, as it involves navigating unknown high-dimensional spaces to establish new verifiable facts or concepts. Additionally, high-throughput automation of experiments (closed-loop) is necessary for tackling high-dimensional problems, which additionally limits SDLs^{28,29}. ML models excel at learning correlations in high-dimensional spaces but struggle with extrapolation and interpretation, especially in the physical sciences where they often act as “black-boxes”, failing to learn the underlying physical principles³⁰⁻³³. This inherently limits the generalizability of ML models since researchers cannot explain ‘why’ a particular discovery makes sense, for instance, in the form of an equation representing the process^{34,35}. Since the advancement of scientific research over the past century has been successful in realizing interpretable solutions by following the scientific method³⁶⁻³⁸, we hypothesize that an ML framework implementing the scientific method can realize interpretable discovery. We therefore envision an SDL to generate high-dimensional experiments, select optimal hypothesis-driven experiments for testing, identify features of relevant optimal experiments, and uncover the relationship between these features and experimental results in an interpretable form. Here, we address two objectives: a) develop a machine-learning framework for autonomous scientific discovery, and b) apply this framework to discover a novel approach to steer spontaneous emission.

To achieve these objectives, we develop an ML framework for autonomous scientific discovery in three steps – specifically to address the needs and limitations of current SDLs:

- a) High dimensionality of inputs: We leverage the manifold hypothesis^{39,40} within the physical sciences, positing that high-dimensional experiments often lie on a low-dimensional manifold. We employ generative models, specifically variational autoencoders (VAEs)⁴¹,

to generate high-dimensional experiments beyond state-of-the-art, from a low-dimensional continuous latent space.

- b) Cost of Experiments: Active learning (AL)¹¹ then selects optimal experiments from the VAE's (low-dimensional) latent space, to develop efficient design of experiments overcoming limitations in exploring high-dimensional spaces. Specifically, active learning predicts the next experiment to be conducted, balancing exploration and exploitation of the input space with appropriate acquisition functions.
- c) Interpretability of Results: Understanding experimental results is crucial, yet generative and active learning models often lack human interpretability. To bridge this gap, we develop a neural network-based equation learners (nn-EQLs) that uncover interpretable equations^{27,42}. Our approach combines the expressive power of neural networks with physics-driven intuition to learn interpretable structure-property relationships through closed-loop experimental feedback.

We apply our ML framework to the problem of steering spontaneous emission, a challenging task with significant potential for clean energy solutions. Spontaneous light emission, as seen in light emitting diodes (LEDs) and thermal lamps, lacks spatio-temporal control, but achieving such control could revolutionize fields like remote sensing and holographic displays⁴³⁻⁴⁹. Traditional methods for controlling coherent (e.g. phased array optics⁵⁰ for lasers) light are not compatible with spontaneous emission. Light-emitting metasurfaces, composed of sub-wavelength periodic arrays of optical resonators with embedded emitters, offer a novel way to control spontaneous emission, and have demonstrated reconfigurable control of spontaneous emission through spatially periodic refractive index modulation⁵¹⁻⁵⁷. However, predicting and controlling emission patterns from aperiodic refractive index modulation remains challenging due to a lack of suitable models and simulation tools. Our approach involves utilizing the ultrafast (<1ps) reconfigurability (through refractive index modulation with optical free-carrier injection) of the metasurface to realize nearly arbitrary phase-array optical elements, mimicking arbitrary high-dimensional spatial index profiles. Our SDL leverages the degrees of freedom enabled by reconfigurability of the metasurfaces to discover the relationship between spatial refractive index profiles and emission patterns through closed-loop, noisy, experimental feedback. Based on the exploration of the AL agent within the latent space of the VAE, we improved the steering efficiency by an order of

magnitude realizing up to 67% over a wide field of view (80°) when compared with state-of-the-art devices⁵⁷, and realized human interpretable equations describing the steering process (Figure 1a). The efficacy of combining generative models with active learning to tackle high-dimensional spaces demonstrates the acceleration of autonomous experimentation platforms towards scientific discovery. Through our approach, we provide a potential pathway for augmenting scientific intuition using neural network equation learners, taking a step beyond scientific discovery to understanding the principles governing spontaneous emission.

Results and Discussion

To rapidly measure spontaneous emission, we develop an automated, closed-loop ultrafast momentum-resolved photoluminescence (PL) measurement setup featuring a reconfigurable GaAs metasurface with embedded, light-emitting, InAs quantum dots, grown epitaxially on a reflective distributed Bragg reflector. The local intensity of the ultrafast optical pump (800 nm, 40 fs pulse-width laser, 2-3 mJ/cm² at 1 kHz) dynamically changes the local refractive index of the GaAs metasurface resonators through free-carrier refraction (Figure 1a). An active learning (AL) agent drives the experiments, sampling the smooth lower-dimensional latent space of a variational

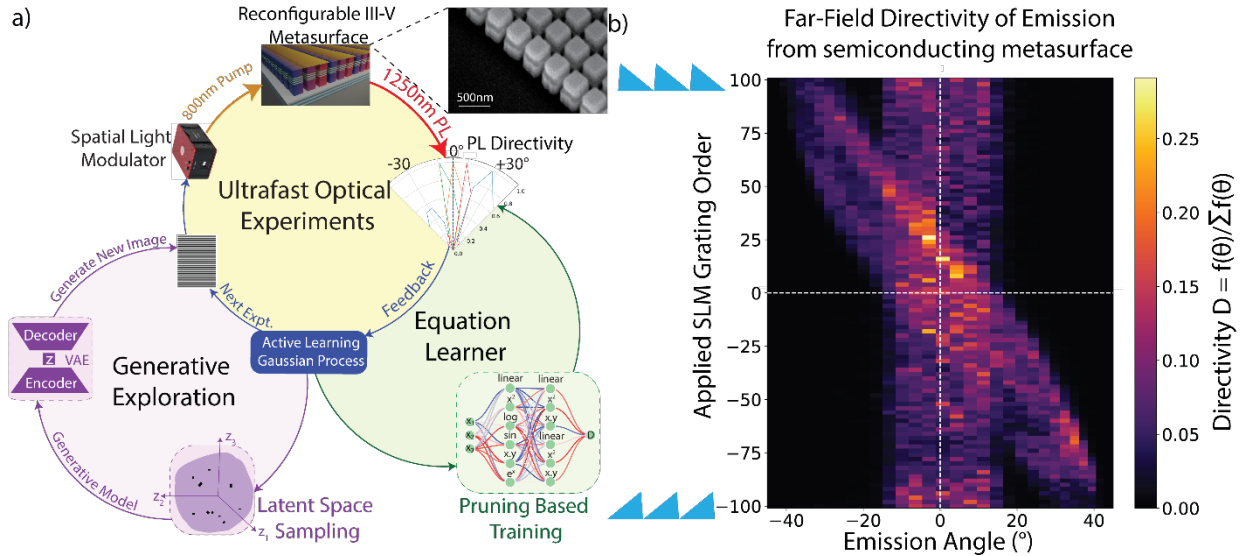


Figure 1: Spontaneous Emission Steering. a) Self-driving lab framework: An active learning agent drives a generative model (variational autoencoder, VAE) and the ultrafast optical experiment. A 40 fs pulsed pump laser at 800 nm images a spatial light modulator onto a reconfigurable metasurface (scanning electron microscope image at the top right). This setup measures the directivity of photoluminescence (PL) from the metasurface with closed-loop feedback. The latent space discovered by the active learning surrogate model is recast as a human-interpretable equation using a neural network-based equation learner. b) Far-field directivity emission from the metasurface under saw-tooth shaped (uniform spatial momentum) pump patterns applied on the SLM, varied from -100 to +100 grating orders. The directivity (D) of emission is defined as the ratio of signal towards a given angle ($f(\theta)$) to the sum of signals over all angles ($\Sigma f(\theta)$)

autoencoder (VAE) to generate new optical pump patterns. These patterns are projected onto the metasurface as intensity patterns using a spatial light modulator (SLM) to realize the spatial refractive index profile on the metasurface. The far-field directivity of the PL is captured using a lock-in detector scanning the back focal plane of the metasurface emitter (see Supplementary Information S1). For this SDL exemplar, the optical pump pattern setting up the spatial index of profile on the metasurface forms the input image (generated by the VAE) for the experiment and far-field intensity distribution of metasurface emission forms the output which is used by the AL agent to generate the next experiment.

The GaAs metasurface is designed to achieve nearly a $0-2\pi$ phase shift in reflection as a function of local optical pump intensity and is fabricated using electron beam lithography and dry etching as described previously in other works^{52,57}. The metasurface shows overlapping peaks in reflection and PL spectra (Figure S1), indicating that optical resonances (peaks in spectra) measured in reflection can enhance the far-field emission from the metasurface. We demonstrate that the metasurface steers light emission (Figure 1b) over an 80° field of view under one-dimensional uniform momentum profiles created by saw-tooth patterns with different spatial frequencies on the optical pump structured using the SLM. Far-field emission directivity measurements ($D = \frac{f(\theta_i)}{\sum_j f(\theta_j)}$, where $f(\theta_i)$ is the steered signal towards angle θ_i) reveal a band of emission between $\pm 14^\circ$ (due to the distributed Bragg reflector substrate) for all applied grating orders, with some emission steered to off-normal angles responding to the pump pattern's spatial momentum. This result (Figure 1b) indicates that only part of the metasurface emission follows the known momentum matching principles of spontaneous light emission steering^{51,52,57-60}. Therefore, ML has the potential to discover better solutions beyond momentum matching principles, solving the inverse problem of predicting the optimal spatial refractive index profile to maximize directivity towards a given angle. In our work, the ML framework controls the closed-loop ultrafast optical experiment to maximize the metasurface emission directivity towards a desired angle.

We first benchmark the components of our ML framework to ensure that the VAE can generate a wide variety of images beyond human intuition⁴¹ and that the AL agent can search over known spaces to rediscover known results. We quantify the generative capability of the VAE by visualizing the local-slope distribution of the optical pump patterns generated by the VAE,

demonstrating that the generated optical pump patterns exceeds the state-of-the-art (training set) by two orders of magnitude (See Methods and Supplementary Information S2). The AL agent begins by using a limited initial training set (optical pump patterns and their associated directivity) to predict directivity across various optical pump patterns. An acquisition function then identifies patterns that could maximize directivity. The ultrafast, automated PL experiment is then performed by projecting this pattern on the metasurface, and the measured result (and associated noise, statistics) is added to the training set of the AL agent. This loop continues until an optimum is reached, or a pre-set experimental budget is reached. We find that the AL agent, when searching over the space of possible grating orders, re-discovers the optimal grating order for steering into a given direction with an order of magnitude fewer number of experiments than brute-force sampling. (See Methods and Supplementary Information S2). Given the success of the AL agent in finding pump patterns described using a single parameter (grating order), we now use AL to find pump patterns described using a complex set of low dimensional features, i.e. the VAE latent space.

In Figure 2a, we show the results of the AL agent maximizing the steered signal towards two different emission angles without prior knowledge (i.e. the AL agent has no prior information of the VAE, the experimental noise, and past results). The AL agent samples the VAE’s latent space,

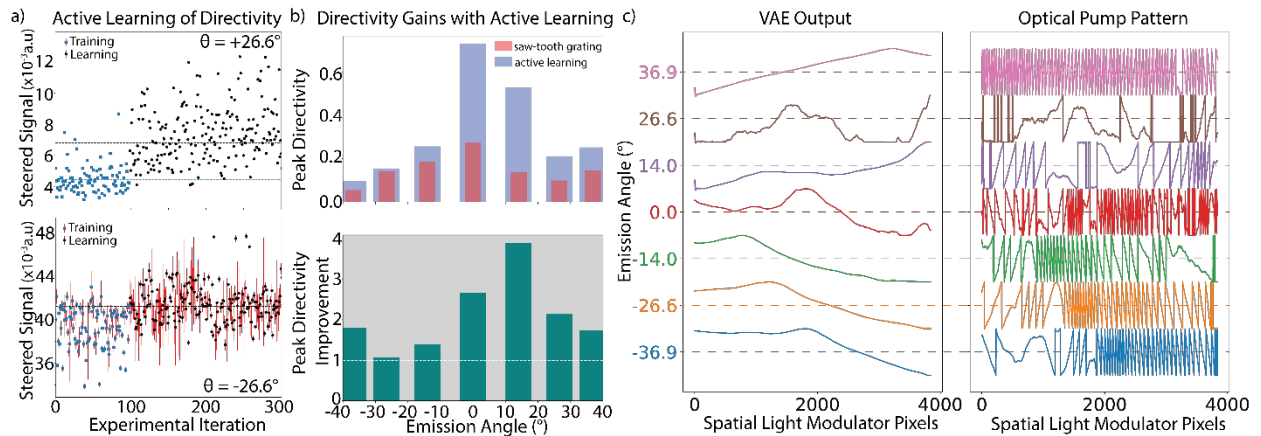


Figure 2: Improving Emission Directivity with Active Learning: a) Top (bottom) panel shows the active learning result for the emission angle at $\pm 26.6^\circ$. Blue dots represent training points (Sobol sampling) in the VAE latent space, and black points represent improved steering signals learned by the active learning agent. The blue dashed line indicates the average of the training points, while the black line indicates the average of the learning points. Red vertical stripes show measurement errors averaged over 10 repeats. b) Relative improvement in steering efficiency by the active learning agent across multiple far-field emission angles through closed-loop experimental feedback. The top panel shows the peak directivity of emission optimized for each far-field angle, with the active learning agent’s values in blue and the saw-tooth grating values in red. The bottom panel shows the relative improvement in peak directivity for different emission angles enabled by the active learning agent. c) Left panel shows the optimal VAE output (normalized) learned by the active learning agent, and the right panel shows the normalized 1-D pump pattern transforming the VAE output for loading into the SLM: $Y_{\text{SLM}} = (Y_{\text{VAE}} \% 2\pi)/2\pi$ for different emission angles.

aiming to maximize directivity while trying to minimize the number of experiments. Each experiment (dot in Figure 2a) starts with the AL agent predicting a point in the VAE's latent space representing a potentially high-directivity curve. This point generates a one-dimensional curve (Y_{VAE} of length 3840) through the VAE decoder, which is transformed into an optical pump pattern in two steps. i) phase wrapping and normalizing the curve to the 8-bit resolution of the SLM to generate $Y_{\text{SLM}} = (Y_{\text{VAE}} \% 2\pi) / 2\pi$; and ii) repeating Y_{SLM} along the orthogonal axis (2160 times) to form a two-dimensional image (3840x2160 pixels) projected onto the metasurface. The noise in the far-field emission has four independent sources: the ultrafast-pulsed laser, SLM, infrared detector, and lock-in amplifier. The directivity of PL is estimated with 10 repeats of the experiment to derive the mean (output) and its standard deviation (noise, See Supplementary information S1). Combining the VAE's enhanced generative capability with the AL agent's efficiency, we maximized the directivity of spontaneous emission from the GaAs metasurface.

We find that the AL agent sampling the VAE's latent space improves peak directivity across a 74° field-of-view within 300 closed-loop iterations without prior knowledge (Figure 2a). Compared to the state-of-the-art saw-tooth grating patterns⁵⁷, the absolute directivity of emission increases by an average of 2.2x (Figure 2b), with a peak improvement of 3.77x at 14.4° . Here, we note that the AL agent utilizes the real-time noise (red error bars in Figure 2a) characteristic of each experiment (See methods) performed by the SDL. Notably, the absolute directivity peak of 67% is one of the highest reported for classical static LEDs, which typically require bulky reflector lenses and collimators to achieve similar directivity⁷⁶. We demonstrate that a dynamically reconfigurable light emitting metasurface can be designed to increase emission directivity based on an aperiodic spatial refractive index pattern imposed on the emitter. The AL agent, leveraging the VAE's generative potential, provides a novel approach to maximize emission directivity, surpassing state-of-the-art methods to achieve comparable performance to commercial LEDs⁷⁶ without additional packaging or bulky optics, while retaining the ability to steer emission over 74° .

Remarkably, we discover that the optimal VAE outputs for different emission angles, as identified by the AL agent, can be described as a combination of the spatial phase profiles of a lens and a grating (Figure 2c). The spatial (x - pixels on SLM) phase (y) profile of an optical lens (used to focus light) is a parabola: $y = ax^2$ (where a represents the lens curvature), while the saw-tooth

gratings (used to deflect light) have a linear phase profile: $y = bx$ (where b defines the deflection angle, with $b = \text{grating order}/3840$ pixels). Thus, the VAE patterns discovered by the AL agent can be described as $Y_{\text{VAE}} = ax^2 + bx$, and the final optical pump pattern on the SLM becomes $Y_{\text{SLM}} = (ax^2 + bx) \% 2\pi / 2\pi$. This finding, enabled by the AL agent exploiting the generative capability of the VAE, surpasses human intuition, which typically relies on momentum matching (or Fourier transform-based) principles. Current methods for steering light depend solely on grating orders (bx) or the linear spatial gradient established by the refractive index or size profile of the metasurface resonators. Here, for the first time, we discover a fundamentally new way to steer light from light-emitting metasurfaces with high directivity through the AL agent.

To formalize our visual insights, we quantify the statistical correlation between the VAE's latent space (z_{1-4}) and the physical properties of the SLM pump pattern (Y_{SLM}): **a**- spatial curvature ($\partial^2 y_{\text{vac}}/\partial x^2$), **b**- spatial gradient ($\partial y_{\text{vac}}/\partial x$), **A**- average pump intensity ($\langle Y_{\text{SLM}} \rangle$), and **ω** - largest spatial frequency ($|\text{FourierTransform}\{Y_{\text{SLM}}\}|_{\text{max}}$). These features are commonly used to describe the spatial refractive index profile of the optical pump pattern. Spearman correlation coefficients⁶⁵,

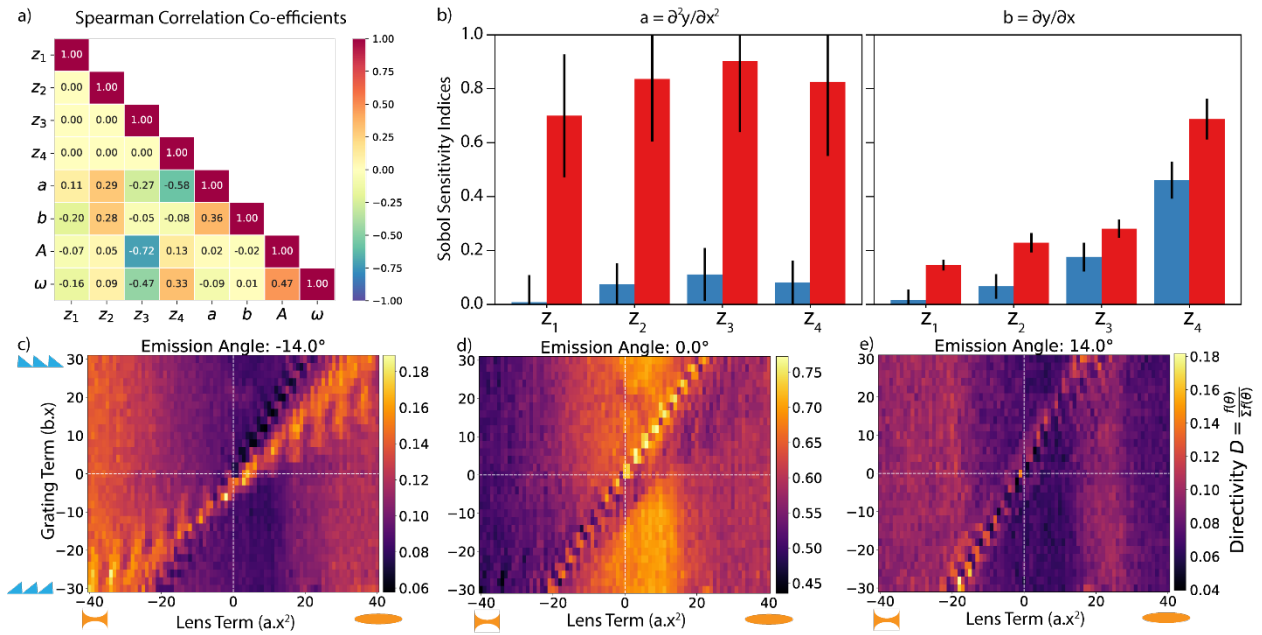


Figure 3: Latent space discovery with active learning. a) Spearman correlation coefficients among latent dimensions learnt by the VAE, a,b-spatial curvature and gradient of the pump,,A, ω -average intensity and the highest spatial frequency of the SLM pump profile. b) Sobol correlations between latent space dimensions of the VAE with the spatial curvature (left panel), and the gradient (right panel) of the optical pump profile. The blue bars indicate correlation with respect to an individual variable (z_i) while the red bars highlight the correlation in the presence of other latent space variables. The black stripes on top of the bars indicates the possible error bar in the correlation statistic. c,d,e) Measured directivity of emission from the metasurface as a function of spatial curvature, a and gradient, b for steering results $-14^\circ, 0$, and $+14^\circ$ respectively.

averaged over 10,000 VAE-generated curves (using Sobol Sampling), reveal: a) \mathbf{z}_4 weakly correlates with the spatial curvature, \mathbf{a} ; b) \mathbf{z}_3 negatively correlates with the average pump intensity, \mathbf{A} ; and c) the VAE's latent space dimensions are orthogonal (See Methods). The rest of the latent space shows no or weak correlation with other physical properties of the pump pattern. While Spearman correlations indicate isolated correlations, Sobol' sensitivity indices⁶⁶⁻⁶⁸ help us understand the combined correlations of multiple latent space variables. These indices show that no single latent space dimension correlates strongly with \mathbf{a} , but combinations of dimensions do. For spatial gradients, only \mathbf{z}_4 correlates weakly in isolation, but a combination of \mathbf{z}_{1-3} and \mathbf{z}_4 correlates strongly with \mathbf{b} . This indicates that the AL agent discovered a correlated sub-space of patterns with high performance across all angles, which are interpretable and tied to physically relevant quantities. We experimentally validate the AL agent's discovery using a parameter sweep on the optical pump pattern (Figure 3c,d,e and Supplementary information S3), finding that specific combinations of lens and grating pump patterns result in high directivity. Combining lens and grating pump patterns creates an aperiodic spatial refractive index profile, dynamically

reconfiguring the metasurface to achieve high directivity. Our work thus reveals a new structure-property relationship governing spontaneous emission steering at the nanoscale, relating aperiodic spatial refractive index (momentum) profiles and directivity beyond current momentum matching principles.

We translate the structure-property relationship discovered by the AL agent and the VAE to a human-interpretable equation describing the directivity (D) of emission as a function of the latent space (a, b) using a neural network-based equation learner (nn-EQL)^{27,42}. The nn-EQL is a two-layer neural network with non-linear activation functions (e.g., addition, t^2 , $\sin(t)$, $\cos(t)$, multiplication). We train the nn-EQL to minimize mean-squared error through backpropagation, while using iterative pruning ($>90\%$ sparsity)⁶⁹, to obtain equation (1), see Figure 4. Details on the nn-EQL setup, and the pruning process are described in Methods and Supplementary Section.

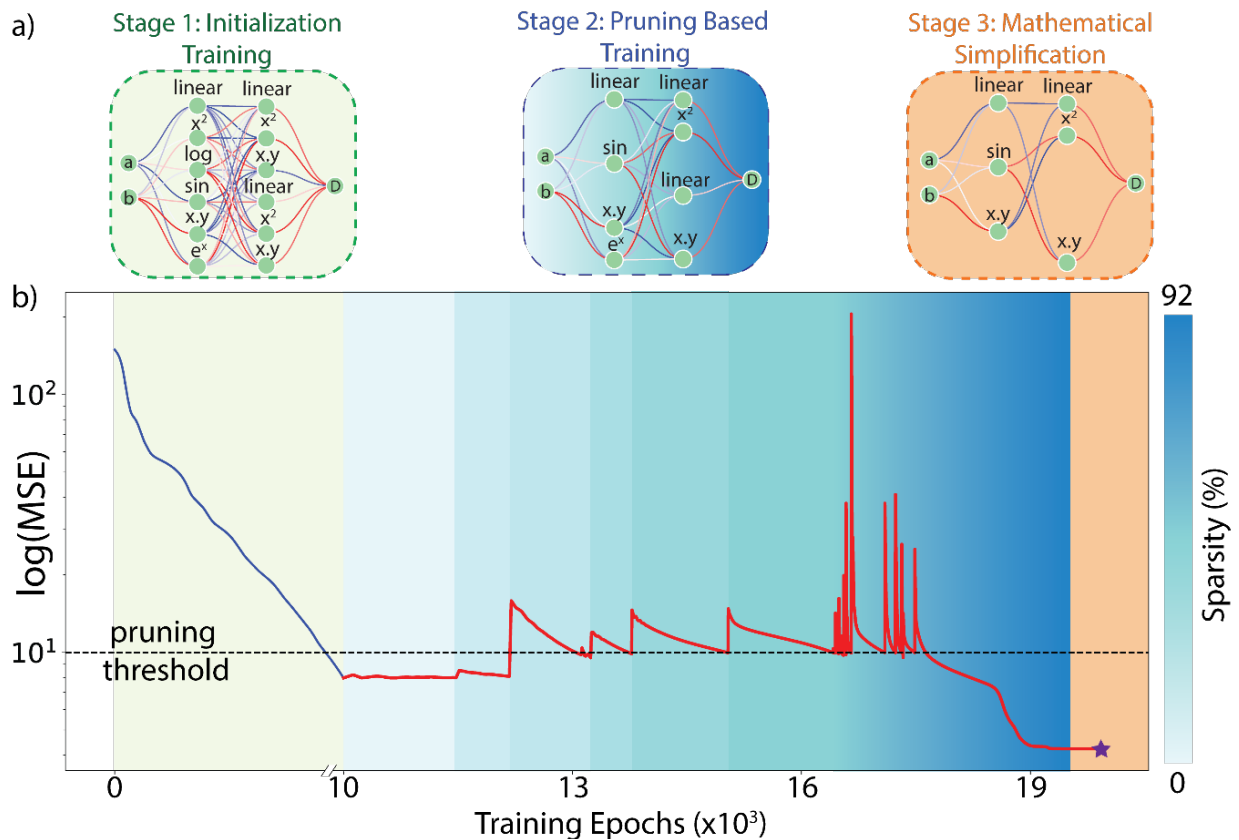


Figure 4: Equation learner framework: a) Our equation learner framework uses a customized neural network with physics-based activation functions defined for each neuron. Stage 1 first performs an initial fit to the dataset, establishing an acceptable error level (green). Stage 2 then iteratively prunes this network, removing neurons that have the lowest contribution in each layer, which is repeated until the highest level (e.g. 90%) of sparsity before the loss terms increases. Finally, Stage 3, we write an equation using the neural network's weights and activation functions and simplify it using sympy⁷⁵ b) The training process (logarithm of the mean squared error of the network vs the training epochs) for generating equations represents the three stages described in figure 4a. The dashed horizontal represents the loss-threshold for initiating the pruning of the least contributing neurons the network. The color bar represents the sparsity progression during the process.

$$D_g(0^\circ) = 0.18(a - 0.033b)^2 + 0.029b^2 + 0.04 \sin(3.52a - 0.04b) + 0.65 \quad (1)$$

The pruned network is readout as an equation and further simplified using Python packages (e.g., sympy). The nn-EQL distilled equation captures the oscillatory behavior observed in the dataset with a ‘ $\sin(3.52a-0.04b)$ ’ term, while ‘ $0.18(a-0.033b)^2$ ’ describes the dependence on spatial curvature. (See Figure 4a and Methods) This equation is a subset of a master equation describing spontaneous emission steering towards 0° concerning the spatial gradient and curvature of the refractive index profile. Repeating this process for other steering orders allows us to develop a generalizable phenomenological model describing light emission from the metasurface.

The spatial refractive index profile, representing a combination of a lens and a grating, presents an intriguing perspective from Fourier optics. Current approaches to steer spontaneous emission rely on momentum matching principles, but our results (Figure 3) and the obtained equation (Figure 4) suggest a new operational principle. This principle considers not only momentum matching (using grating orders, **b**) but also the gradient of momentum (spatial curvature of the index, **a**), akin to lens-like characteristics. For instance, in Figure 3c, combining positive lens (**a**) and positive grating (**b**) values steers light effectively (high directivity) in the first quadrant. However, combining a positive lens with a negative grating (fourth quadrant) shows no steering. In classical optics, a positive lens collimates an LED source, followed by a grating to steer the emission. The ML framework enables combining the lens and grating into a single optic on the light-emitter itself. Negative grating orders combined with positive lens characteristics (fourth quadrant) completely remove the capacity to steer light for all angles, contrary to classical optics. The second and third quadrants of Figure 3c present an even more intriguing scenario where a negative (concave) lens with embedded emitters can steer light in the far-field with an additional negative grating order. A negative lens typically increases the divergence of incident light, counterintuitive to collimating a diverging source unless the source was initially converging. Multiple sets of light emission pathways trapped in the substrate may be out-coupled into free-space along the measurement direction, but further modeling of the system is necessary to verify this possibility. The equivalence in performance between positive and negative lenses (with their corresponding gratings) for steering light emission in the far-field suggests that observed spontaneous light-matter interactions surpass classical Fourier optics' understanding based only on momentum matching.

In summary, we demonstrate a self-driving nanophotonics lab capable of uncovering and elucidating novel structure-property relationships in nanoscale light-matter interactions. Our approach integrates a generative model (VAE), an active learning agent, and an equation learner network, constituting the core elements of a self-driving lab. Leveraging the VAE's capacity to generate patterns beyond human intuition from a condensed design space representation, the active learning agent efficiently optimizes for the metasurface's operational property (directivity of emission) using closed-loop feedback to minimize experimental iterations. The patterns unearthed by the active learning agent across multiple emission angles revealed new latent space variables (such as spatial curvature of the refractive index), enhancing control over spontaneous emission directivity. The nn-EQL distills the active learning agent's discovery into concise equations, offering much-needed human interpretability to machine-learning models. The active learning agent identified optical pump patterns from the VAE, steering spontaneous emission from resonant metasurfaces 2.2x more effectively than human-intuition-driven saw-tooth pump patterns over a 74° field of view, peaking at 67% at normal incidence. We discovered that a spatial index profile formed by combining a lens and a grating outperforms a grating profile alone in steering spontaneous light emission. Specifically, the agent unveiled that these optical components (lens and grating) may be amalgamated into a single phase-space optical pump pattern on a metasurface, transcending current understanding based on Fourier optics. Moreover, we discover a concise structure-property relationship linking the spatial refractive index profile to emission directivity as an equation, facilitating the realization of energy-efficient spontaneous light sources (such as LEDs, thermal lamps, etc.). We anticipate that the methodologies and outcomes demonstrated herein to establish a self-driving ultrafast nanophotonics lab could be generalizable to other physical sciences. This approach has the potential to overcome limitations of human intuition and theoretical frameworks, leveraging generative machine-learning frameworks to drive new scientific discoveries.

Methods

Variational Autoencoder (VAE): We train a VAE to generate arbitrary pump patterns, represented as one-dimensional curves of length 3840 pixels. Given a pump pattern X , a VAE encodes this pump pattern into a low-dimensional latent space representation Z , using an encoder network that learns the distribution $Q(Z|X)$. In this work, we use a latent space representation of size three,

making the latent space a three-dimensional Gaussian distribution. During training, the accuracy of the learnt latent representation Z is determined in part by the ability of the VAE to reconstruct the input pump pattern X , from the latent space representation Z . The VAE achieves this reconstruction by using a decoder network that learns $P(X|Z)$. In this work, we use six fully connected layers for the encoder and the decoder. The objective of the VAE during training is to minimize Evidence Lower Bound (ELBO) loss:

$$L_{VAE} = ||\hat{X} - X||_2^2 + KL(Q(Z|X) || p(Z))$$

Here, the first term is the L2-norm between the set of reconstructed pump patterns \hat{X} , and the set of ground truth patterns X . The second term is a KL-divergence that measures the difference between the encoder-learned distribution $Q(Z|X)$, and the prior distribution $p(Z)$, assumed here to be $N(0, I)$. Once the VAE is trained, new pump patterns are generated by sampling the learned latent space of the VAE. The generated pump patterns are then transformed into two-dimensional images by repeating the intensity of the pump pattern along the y-axis. These images are projected onto the SLM for evaluation of spontaneous emission steering. The training set for the VAE encompasses both grating-order based periodic patterns and aperiodic patterns comprising multiple frequencies and linear/quadratic curves. In total, 50,000 one-dimensional pump patterns are used for VAE training, using the Pytorch package⁷⁰ and the Adam optimizer⁷¹ for training. See Supplementary Information for benchmarking of the generative capability of our trained VAE.

Active Learning on the Latent Space of the Generative Model: We search for optimal pump patterns by navigating the latent space of the trained VAE using active learning. Each point in the latent space represents a pump pattern (obtained using the VAE’s decoder network), and active learning efficiently searches the latent space (i.e., the space of pump patterns that could be generated by the VAE) to find optimal pump patterns. We define optimal pump patterns as patterns with high directivity $D = \frac{f(\theta_i)}{\sum_j(f(\theta_j))}$, i.e., patterns that steer emission maximally in a desired direction θ_i , while minimally steering emission to other angles. Active learning begins with an initial dataset of pump patterns and associated directivity (D) values. This set of pump patterns is chosen by choosing points in the latent space using Sobol’ sampling and using the VAE’s decoder to obtain pump patterns. Directivity is measured using the automated experimental setup (see Supplementary Information), along with uncertainty. We assume the directivity measurement is

assumed to contain errors from the pump power (combining modulation and laser measurement) ΔP , and the thermal noise of the detector ΔS . The uncertainty in the directivity is thus calculated as $\frac{\Delta D}{D} = \sqrt{\frac{\Delta P^2}{P} + \frac{\Delta S}{S}}$. Using this initial dataset, a Gaussian process model GP predicts directivity, with uncertainty, across the latent space, i.e., $D(z) = GP(\mu(z), K(z, z'))$; where z is a point in the latent space of the VAE, $\mu(z)$ is the average directivity for the pump pattern represented in the VAE dimension as z , and $K(z, z')$ is a kernel function representing covariance in directivity between two pump patterns represented as latent space points z and z' . See ⁷² for more details on Gaussian process models. The directivity prediction from the Gaussian process model, along with uncertainty, is used for determining the next experiment that will be conducted. The next experiment z^* is determined by an acquisition function, such as Expected Improvement (EI), with the intention balancing exploration and exploitation in the latent space. Specifically, the next experiment with the EI acquisition function is chosen as: $z^* = \operatorname{argmax} E(\max(GP(z) - GP(z^{curr})), 0)$, where z^{curr} is the point in the latent space with the best directivity so far, and z is any point in the latent space. The EI acquisition function thus chooses the next experiment to be conducted at a latent space z^* where the Gaussian process model predicts the highest improvement in directivity, compared to the best point predicted so far. In this work we use the Ax package⁷³ for the active learning, using 100 points in the latent space as the initial dataset (sampled using Sobol' sampling⁷⁴). Subsequently, 1000 experiments are conducted using the EI acquisition to find optimal pump patterns.

Analyzing Correlations in Latent Space: Correlations in latent space are analyzed using Spearman correlations and Sobol' sensitivity indices. Spearman correlation is defined as: $\rho_{a,b} = \frac{\operatorname{cov}(r_a, r_b)}{\operatorname{var}(r_b)\operatorname{var}(r_b)}$ where r_i is the rank of variable i (highest value is rank 1). Spearman correlations range between -1 and 1 and indicate correlations between pairs of variables. Moving beyond pairs of variables in isolation, Sobol' sensitivity indices indicate the effect of sets of variables on a quantity of interest. Sobol' sensitivity indices are of two types: first-order sensitivity indices, and total-order sensitivity indices. First-order sensitivity indices are defined as: $S_{1,i} = \frac{\operatorname{var}_{X_i}(E_{X \neq X_i}(Y|X_i))}{\operatorname{var}(Y)}$ and measure the variance in the quantity of interest Y when varying one variable

X_i , and averaging over all other variables. Total-order sensitivity indices are defined as: $S_{T,i} = \frac{E_{X_{\sim i}}(\text{var}_{X_i}(Y|X_{\sim i}))}{\text{var}(Y)}$ and are the variance in the quantity of interest as combinations of $\{X_i\}$ are varied.

Equation Learner Network: To distill active learning experiments into an interpretable form, we employ a custom equation learner network (EQL). The EQL is formulated as a dense feed-forward neural network (we use Pytorch⁷⁰) with custom activation functions applied to each neuron. These custom activation functions are inspired from terms present in equations in the physical sciences (sin, cos, exp, product etc.). The EQL is trained in three stages: (1) A two-layer network is trained to achieve an accurate fit to the data (without overfitting) (2) The trained network is pruned to a smaller network that achieves similar accuracy to the network trained in stage 1. We prune the EQL by removing weights with the least ‘contribution’ in each layer, followed by re-training for a few epochs to allow other weights to adjust to the removal of weights with the least contribution. Contribution here is defined as the product of the weight value and the value of the neuron activation from the previous layer. We use contribution as a metric instead of conventional magnitude-based pruning approaches⁶⁹ to account for non-custom activation functions which are not monotonic with weight values (e.g. cos) (3) The pruned network is read-out in terms of human-readable equation using packages such as SymPy⁷⁵.

Coupling Experiments with Powerful Computing Platforms: Our self-driving lab is driven by a laboratory computer capable of instrument control via a Python API. To overcome computational limitations, active learning is performed on a GPU machine with four Tesla V100s, while experimental instruments are controlled via a laboratory computer.

Acknowledgment

This paper describes objective technical results and analysis. Any subjective views or opinions that might be expressed in the paper do not necessarily represent the views of the U.S. Department of Energy or the United States Government. This work was supported in part by the U.S. Department of Energy, Office of Basic Energy Sciences, Division of Materials Sciences and Engineering (BES20017574) and, in part supported by Sandia National Labs’ Laboratory Directed Research and Development program (#230710) and performed in part, at the Center for Integrated Nanotechnologies, an Office of Science User Facility operated for the U.S. Department of Energy (DOE) Office of Science. Sandia National Laboratories is a multi-mission laboratory managed and

operated by National Technology and Engineering Solutions of Sandia, LLC, a wholly owned subsidiary of Honeywell International, Inc., for the U.S. Department of Energy's National Nuclear Security Administration under contract DE-NA0003525.

References

1. Flores-Leonar, M. M. *et al.* Materials Acceleration Platforms: On the way to autonomous experimentation. *Curr Opin Green Sustain Chem* **25**, (2020).
2. Hickman, R. J., Bannigan, P., Bao, Z., Aspuru-Guzik, A. & Allen, C. Self-driving laboratories: A paradigm shift in nanomedicine development. *Matter* **6**, 1071–1081 (2023).
3. Lo, S. *et al.* Review of low-cost self-driving laboratories in chemistry and materials science: the “frugal twin” concept. *Digital Discovery* (2024) doi:10.1039/D3DD00223C.
4. MacLeod, B. P. *et al.* A self-driving laboratory advances the Pareto front for material properties. *Nat Commun* **13**, (2022).
5. MacLeod, B. P. *et al.* Self-driving laboratory for accelerated discovery of thin-film materials. *Sci Adv* **6**, (2020).
6. Häse, F., Roch, L. M. & Aspuru-Guzik, A. Next-Generation Experimentation with Self-Driving Laboratories. *Trends Chem* **1**, 282–291 (2019).
7. BP MacLeod, F. P. A. B. J. H. C. B. Flexible automation accelerates materials discovery. *Nat. Mater.* **21**, 722–726 (2022).
8. The rise of self-driving labs in chemical and materials sciences | Nature Synthesis. <https://www.nature.com/articles/s44160-022-00231-0>.
9. Seifrid, M. Autonomous chemical experiments: challenges and perspectives on establishing a self-driving lab. *Acc. Chem. Res.* **55**, 2454–2466 (2022).
10. Tabor, D. Accelerating the discovery of materials for clean energy in the era of smart automation. *Nat. Rev. Mater.* **3**, 5–20 (2018).
11. Gongora, A. A Bayesian experimental autonomous researcher for mechanical design. *Sci. Adv.* **6**, eaaz1708 (2020).
12. Deneault, J. R. *et al.* Toward autonomous additive manufacturing: Bayesian optimization on a 3D printer. *MRS Bull* **46**, 566–575 (2021).
13. Szymanski, N. J. *et al.* An autonomous laboratory for the accelerated synthesis of novel materials. *Nature* **624**, 86–91 (2023).
14. Bateni, F. Autonomous nanocrystal doping by self-driving fluidic micro-processors. *Adv. Intell. Syst.* **4**, 2200017 (2022).
15. Seifrid, M. *et al.* Autonomous Chemical Experiments: Challenges and Perspectives on Establishing a Self-Driving Lab. *Acc. Chem. Res.* **55**, 2454–2466 (2022).
16. Porwol, L. An autonomous chemical robot discovers the rules of inorganic coordination chemistry without prior knowledge. *Angew. Chem. Int. Ed.* **59**, 11256–11261 (2020).
17. Abdel-Latif, K. *et al.* Self-Driven Multistep Quantum Dot Synthesis Enabled by Autonomous Robotic Experimentation in Flow. *Adv. Intell. Syst.* **3**, (2021).
18. Sagmeister, P. Autonomous multi-step and multi-objective optimization facilitated by real-time process analytics. *Adv. Sci.* **9**, 2105547 (2022).
19. Nikolaev, P. Autonomy in materials research: a case study in carbon nanotube growth. *npj Comput. Mater.* **2**, 16031 (2016).
20. Christensen, M. *et al.* Data-science driven autonomous process optimization. *Commun Chem* **4**, (2021).
21. AA Volk, M. A. Autonomous flow reactors for discovery and invention. *Trends Chem.* **3**, 519–522 (2021).
22. Shimizu, R., Kobayashi, S., Watanabe, Y., Ando, Y. & Hitosugi, T. Autonomous materials synthesis by machine learning and robotics. *APL Mater* **8**, (2020).

23. W Gao, P. R. C. C. Autonomous platforms for data-driven organic synthesis. *Nat. Commun.* **13**, (2022).
24. Manzano, J. S. *et al.* An autonomous portable platform for universal chemical synthesis. *Nat. Chem.* **14**, 1311–1318 (2022).
25. Stach, E. *et al.* Autonomous experimentation systems for materials development: a community perspective. *Matter* **4**, 2702–2726 (2021).
26. Volk, A. A. & Abolhasani, M. Performance metrics to unleash the power of self-driving labs in chemistry and materials science. *Nat Commun* **15**, (2024).
27. Desai, S. & Strachan, A. Parsimonious neural networks learn interpretable physical laws. *Sci Rep* **11**, (2021).
28. Kusne, A. G. *et al.* On-the-fly closed-loop materials discovery via Bayesian active learning. *Nat. Commun.* **11**, 5966 (2020).
29. Angello, N. H. *et al.* Closed-loop optimization of general reaction conditions for heteroaryl Suzuki-Miyaura coupling. *Science (1979)* **378**, 399–405 (2022).
30. Linardatos, P., Papastefanopoulos, V. & Kotsiantis, S. Explainable AI: A Review of Machine Learning Interpretability Methods. *Entropy 2021, Vol. 23, Page 18* **23**, 18 (2020).
31. Doshi-Velez, F. & Kim, B. Towards A Rigorous Science of Interpretable Machine Learning. (2017).
32. Gilpin, L. H. *et al.* Explaining explanations: An overview of interpretability of machine learning. *Proceedings - 2018 IEEE 5th International Conference on Data Science and Advanced Analytics, DSAA 2018* 80–89 (2018) doi:10.1109/DSAA.2018.00018.
33. Goldstein, A., Kapelner, A., Bleich, J. & Pitkin, E. Peeking Inside the Black Box: Visualizing Statistical Learning With Plots of Individual Conditional Expectation. *Journal of Computational and Graphical Statistics* **24**, 44–65 (2015).
34. Du, M., Liu, N. & Hu, X. Techniques for interpretable machine learning. *Commun ACM* **63**, 68–77 (2020).
35. Rudin, C. Stop explaining black box machine learning models for high stakes decisions and use interpretable models instead. *Nat Mach Intell* **1**, 206–215 (2019).
36. Tsao, J. Y. *et al.* AI for Technoscientific Discovery: A Human-Inspired Architecture. *Journal of Creativity* **34**, 100077 (2024).
37. Narayanamurti, V. & Tsao, J. Y. How technoscientific knowledge advances: A Bell-Labs-inspired architecture. *Res Policy* **53**, 104983 (2024).
38. Narayanamurti, V. & Tsao, J. Y. The genesis of technoscientific revolutions rethinking the nature and nurture of research.
39. Narayanan, H. & Mitter, S. Sample Complexity of Testing the Manifold Hypothesis. *Adv Neural Inf Process Syst* **23**, (2010).
40. Fefferman, C., Mitter, S. & Narayanan, H. Testing the manifold hypothesis. *Journal of the American Mathematical Society* **29**, 983–1049 (2016).
41. Mahmud, M. S., Huang, J. Z. & Fu, X. Variational Autoencoder-Based Dimensionality Reduction for High-Dimensional Small-Sample Data Classification. *Int J Comput Intell Appl* **19**, (2020).
42. Sahoo, S. S., Lantpert, C. H. & Martius, G. Learning Equations for Extrapolation and Control. *35th International Conference on Machine Learning, ICML 2018* **10**, 7053–7061 (2018).
43. Greffet, J.-J. *et al.* Coherent emission of light by thermal sources. *Nature* **416**, 61–64 (2002).

44. Guo, Y., Cortes, C. L., Molesky, S. & Jacob, Z. Broadband super-Planckian thermal emission from hyperbolic metamaterials. *Appl Phys Lett* **101**, 131106 (2012).
45. Liberal, I. & Engheta, N. Tailoring Thermal Emission with Epsilon-Near-Zero Media Augmented with Dielectric Rods. in *Conference on Lasers and Electro-Optics* FM4G.3 (OSA, Washington, D.C., 2017). doi:10.1364/CLEO_QELS.2017.FM4G.3.
46. Dyachenko, P. N. *et al.* Controlling thermal emission with refractory epsilon-near-zero metamaterials via topological transitions. *Nat Commun* **7**, 11809 (2016).
47. Song, W. *et al.* 3D Holographic Displays: Large-Scale Huygens' Metasurfaces for Holographic 3D Near-Eye Displays (Laser Photonics Rev. 15(9)/2021). *Laser Photon Rev* **15**, 2170047 (2021).
48. David, A., Benisty, H. & Weisbuch, C. Optimization of Light-Diffracting Photonic-Crystals for High Extraction Efficiency LEDs. *Journal of Display Technology* **3**, 133–148 (2007).
49. Krames, M. R. *et al.* Status and Future of High-Power Light-Emitting Diodes for Solid-State Lighting. *Journal of Display Technology* **3**, 160–175 (2007).
50. Park, J. *et al.* All-solid-state spatial light modulator with independent phase and amplitude control for three-dimensional LiDAR applications. *Nature Nanotechnology* 2020 16:1 **16**, 69–76 (2020).
51. Iyer, P. Unidirectional luminescence from InGaN/GaN quantum-well metasurfaces. *Nat. Photon.* **14**, 543–548 (2020).
52. Iyer, P. P., Desai, S., Addamane, S., Dingreville, R. & Brener, I. Learning Incoherent Light Emission Steering From Metasurfaces Using Generative Models. 3770–3777 Preprint at (2023).
53. Langguth, L., Schokker, A. H., Guo, K. & Koenderink, A. F. Plasmonic phase-gradient metasurface for spontaneous emission control. *Phys Rev B* **92**, 205401 (2015).
54. Liu, S. *et al.* Light-Emitting Metasurfaces: Simultaneous Control of Spontaneous Emission and Far-Field Radiation. *Nano Lett* **18**, 6906–6914 (2018).
55. Lodahl, P. *et al.* Controlling the dynamics of spontaneous emission from quantum dots by photonic crystals. *Nature* **430**, 654–657 (2004).
56. Mohtashami, Y. *et al.* Light-emitting metalenses and meta-axicons for focusing and beaming of spontaneous emission. *Nature Communications* 2021 12:1 **12**, 1–7 (2021).
57. Iyer, P. P. *et al.* Sub-picosecond steering of ultrafast incoherent emission from semiconductor metasurfaces. *Nature Photonics* 2023 17:7 **17**, 588–593 (2023).
58. Heki, L. *et al.* Designing Highly Directional Luminescent Phased-Array Metasurfaces with Reciprocity-Based Simulations. *ACS Omega* **7**, 22477–22483 (2022).
59. Heki, L. K. *et al.* Optimizing Polarization Selective Unidirectional Photoluminescence from Phased-Array Metasurfaces. *Adv Opt Mater* **12**, 2303186 (2024).
60. Mohtashami, Y. *et al.* Metasurface Light-Emitting Diodes with Directional and Focused Emission. *Nano Lett* **23**, 10505–10511 (2023).
61. Svilainis, L. LEDs for large displays. *Nitride Semiconductor Light-Emitting Diodes (LEDs): Materials, Technologies, and Applications: Second Edition* 659–736 (2018) doi:10.1016/B978-0-08-101942-9.00021-6.
62. Svilainis, L. & Dumbrava, V. Numerical comparison of LED directivity approximation functions for video displays. *Displays* **31**, 196–204 (2010).
63. Svilainis, L. LED directivity measurement in situ. *Measurement* **41**, 647–654 (2008).

64. Chen, Q., Hu, R. & Luo, X. A statistical study to identify the effects of packaging structures on lumen reliability of LEDs. *Microelectronics Reliability* **71**, 51–55 (2017).
65. Spearman, C. The Proof and Measurement of Association between Two Things. *Am J Psychol* **15**, 72 (1904).
66. Homma, T., Safety, A. S.-R. E. & S. & 1996, undefined. Importance measures in global sensitivity analysis of nonlinear models. *ElsevierT Homma, A SaltelliReliability Engineering & System Safety, 1996•Elsevier* **52**, 17 (1996).
67. IM Sobol. On sensitivity estimation for nonlinear mathematical models. *Math. Model. Comput. Exp* **407**, (1993).
68. Sobol, I. M. Global sensitivity indices for nonlinear mathematical models and their Monte Carlo estimates. *Math Comput Simul* **55**, 271–280 (2001).
69. Frankle, J. & Carbin, M. The lottery ticket hypothesis: Finding sparse, trainable neural networks. *7th International Conference on Learning Representations, ICLR 2019* (2019).
70. Paszke, A. *et al.* PyTorch: An Imperative Style, High-Performance Deep Learning Library. *Adv Neural Inf Process Syst* **32**, (2019).
71. Kingma, D. P. & Ba, J. L. Adam: A Method for Stochastic Optimization. *3rd International Conference on Learning Representations, ICLR 2015 - Conference Track Proceedings* (2014).
72. Rasmussen, C. E. Gaussian Processes in machine learning. *Lecture Notes in Computer Science (including subseries Lecture Notes in Artificial Intelligence and Lecture Notes in Bioinformatics)* **3176**, 63–71 (2004).
73. Bakshy, E. *et al.* AE: A domain-agnostic platform for adaptive experimentation. *eytan.github.ioE Bakshy, L Dworkin, B Karrer, K Kashin, B Letham, A Murthy, S SinghConference on neural information processing systems, 2018•eytan.github.io*
74. Sobol', I. M. On the distribution of points in a cube and the approximate evaluation of integrals. *USSR Computational Mathematics and Mathematical Physics* **7**, 86–112 (1967).
75. Meurer, A., Smith, C., Paprocki, M., ... O. Č.-P. C. & 2017, undefined. SymPy: symbolic computing in Python. *peerj.comA Meurer, CP Smith, M Paprocki, O Čertík, SB Kirpichev, M Rocklin, AMT Kumar, S IvanovPeerJ Computer Science, 2017•peerj.com*.
76. Tsao, J. Y., Crawford, M. H., Coltrin, M. E., Fischer, A. J., Koleske, D. D., Subramania, G. S., ... & Karlicek Jr, R. F. (2014). Toward smart and ultra-efficient solid-state lighting. *Advanced Optical Materials*, 2(9), 809-836.

Supplementary Information

Self-driving lab discovers principles for steering spontaneous emission

Saaketh Desai, Sadhvikas Addamane, Jeffery Y. Tsao, Igal Brener, Remi Dingreville, Prasad P. Iyer*

Center for Integrated Nanotechnologies, Sandia National Lab, Albuquerque NM, USA

ppadma@sandia.gov

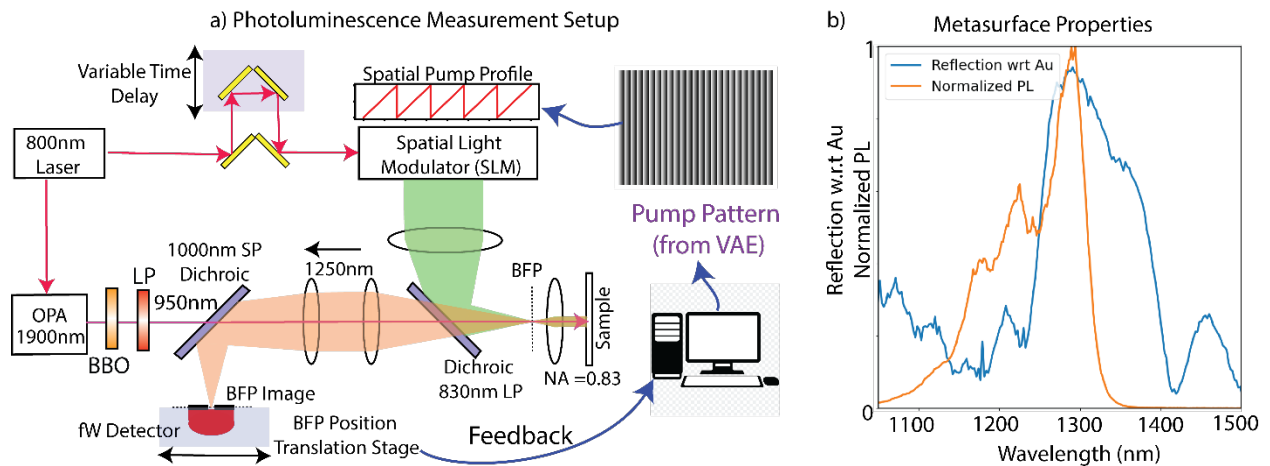
Table of Contents

1. Ultra-fast optical dual pump experiment and Semiconductor Metasurface Properties
2. Benchmarking the ML models
 - a. Generative capability of the VAE
 - b. Efficiency of the active learning
 - c. Equation learner network fit
3. Steering over wide field of view with lens and grating

1. Ultra-fast optical dual pump experiment and Semiconductor Metasurface Properties

We steer incoherent light from a reconfigurable semiconductor (GaAs) metasurface under structured optical pumping, see Figure S1a. We design the metasurface resonance to achieve reconfigurable phase response in reflection under free-carrier excitation (with optical pumping). Additionally, the metasurface resonances are aligned to the embedded InAs quantum dot emitters ($\lambda_e = 1280\text{nm}$) such that the photoluminescence (PL) peak and the reflection peak are spectrally overlapping. The metasurfaces were designed such that under the influence of the optical pump induced refractive index change, the phase (ϕ) of the light in reflection undergoes a $0 - 2\pi$ phase shift with minimal change in the amplitude. We demonstrate that this design criteria constructed for coherent reflection translates into momentum change for the light emission under spatially structured optical pumping. The GaAs metasurfaces were grown with a reflective distributed Bragg grating made up of 15 pairs of $\text{Al}_{0.3}\text{Ga}_{0.7}\text{As}$ and AlAs layers with $\lambda_e/4n$ thicknesses, where n is the refractive index of each of the layer (3.2 and 2.94 respectively) at the emission wavelength^{1,2}. InAs quantum dots (QDs) were also epitaxially grown within the top GaAs layer as dot in a well (DWELL) configuration.³ The metasurfaces were fabricated using traditional nano-fabrication techniques which included:

- Electron beam lithography to define the metasurface resonator shape (width = 280nm) and periodicity (400nm).
- Deposition and lifted-off an Al_2O_3 hard mask of 25nm.
- Dry etching 675nm of the top GaAs layer using a Cl_2 gas etch chemistry.



d) Verifying the fabrication process using scanning electron microscope images, see Figure 1a. The ultrafast optical pump at 800nm, made up of 80fs pulses repeating at 1KHz (Coherent Astrella Laser system with TOPAS OPA), is reflected of a spatial light modulator (SLM) and the intensity profile from the image loaded on the SLM is projected onto the reconfigurable metasurface. The 800nm pump optical excites free carriers in the resonator and the quantum dots resulting in incoherent emission and refractive index change. We generate a 950nm (80fs pulse width and 1KHz repetition rate), by passing part of the 800nm pulse through an optical parametric amplifier (OPA) to generate an idler beam at 1900nm which is frequency doubled using a BBO-crystal, to only pump the QDs in the metasurface and estimate the temporal evolution of the PL. The light emission from the metasurface is imaged in the back-focal-plane using a single pixel (InGaAs detector) using lock-in amplifier setup. We measure the modulation signal at the sum frequency of the modulation of both 800nm and 950nm beam which modulated using a single chopper (5/7 relatively prime modulation) at 2 frequencies. The dual chop lock-in to the sum of the chopping frequency enables us to reduce the noise in the steering measurements^{4,5,6}. We use a series of dichroic (830nm long pass at 45°), short-pass (1550nm short pass) and long-pass (1150nm, 1200nm long pass) filters to ensure that we are only collecting the PL signal from the metasurface. The PL directivity is measured by scanning the detector in the back-focal-plane for a given image projected onto the sample. Further details of the measurement setup and metasurface design can be found here^{52,57}.

2. Benchmarking the Machine Learning models

a. **Generative capability of the VAE:** The role of the generative model in our self-driving lab is to generate novel pump patterns beyond pump patterns currently explored in state-of-the-art experiments. In this work we use a VAE as our generative model, and to capture the generative capability of our VAE, we quantify the distribution of local slopes in the pump patterns generated by the VAE, see Figure S2. The local slope of a pump pattern y is defined as dy/dx , where x is the pixel index, i.e., the axis along which the intensity changes. Each pump pattern will thus have a distribution of local slopes, representing the variation in pump pattern intensity as a function of pixel location. Figure S2 shows that state-of-the-art sawtooth (grating order) pump patterns (green) have a narrow slope range, limited by assuming a fixed (sawtooth) functional form the pump patterns. The range of local slopes in the training set of the VAE (orange) is wider than the sawtooth

patterns but is again limited by the assumption of a few fixed functional forms. The slopes of the patterns generated by the VAE (blue) are much broader than both the training set and the state-of-the-art sawtooth patterns, confirming that the VAE generates novel patterns beyond human intuition.

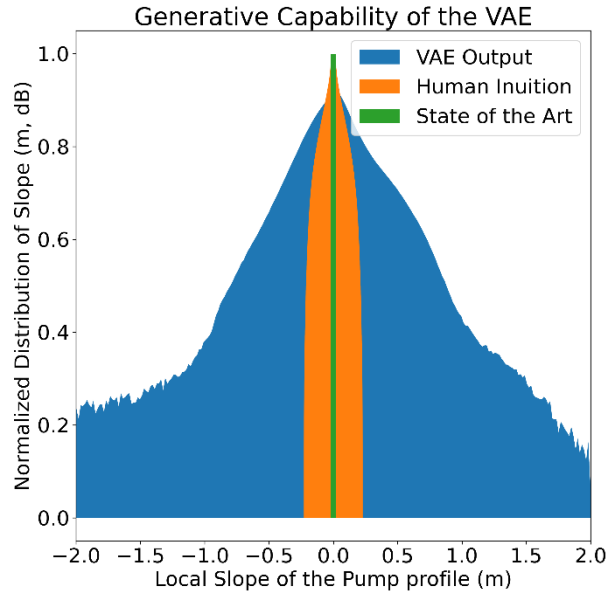


Figure S2: Generative Capability of the VAE. The normalized distribution (log scale) of the local slope (m) in the optical pump patterns imaged on to the metasurface. Green represents the saw-tooth patterns which were used in the state-of-the-art demonstration of incoherent emission steering. Orange represents human intuition-based VAE training set, while blue represents the local slope distribution from the output of the VAE.

b. **Efficiency of active learning:** The role of active learning in our self-driving lab is to discover pump patterns that have optimal performance, as measured by directivity. To benchmark active learning, we demonstrate a simple one-dimensional optimization, searching over the space sawtooth patterns with varying frequency (grating order) to find the sawtooth pattern with highest intensity at a specific angle. We choose this problem as prior work has a documented a solution, discovering that sawtooth pump patterns with grating order of +80 steer the most signal to a specific angle. This discovery was made using brute force iteration over 160 grating orders, and Figure S3 shows that active learning can re-discover this result using an order of magnitude (~ 20) experiments. In other words, active learning is an efficient way to guide experiments towards

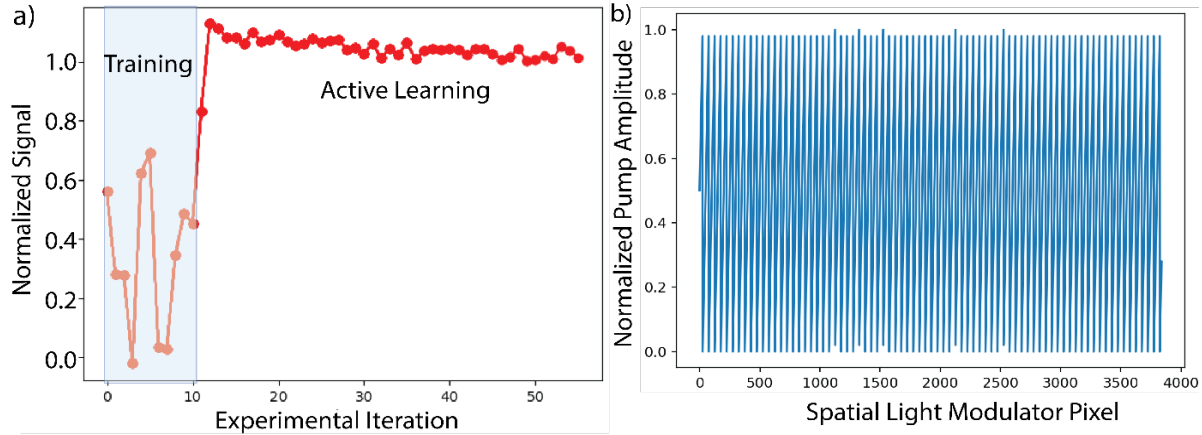


Figure S3. Efficiency of Active Learning for one dimensional problem. a) Normalized PL signal measured with the active learning optimizing over grating orders. Active learning is rediscovering a known result with 10% the number of experimental iterations required for a brute force search at an emission angle of -37° . b) The plot shows the normalized pump amplitude at the end of the active learning process, corresponding to a grating order of 80.

suitable pump patterns such that we discover optimal grating order patterns with minimal experiments, avoiding brute force parameter sweeps.

3. Equation learner network fits

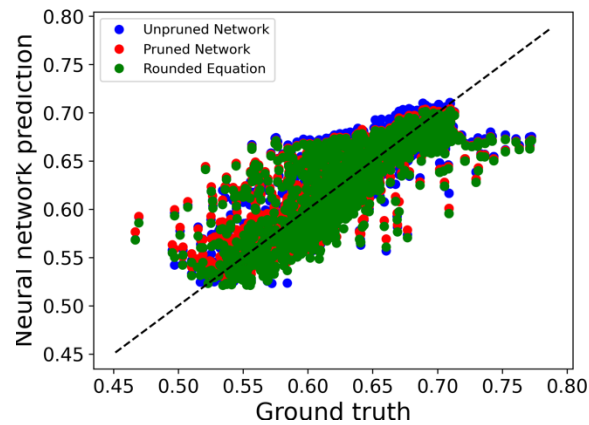


Figure S4. Parity plot from the nn-EQL. Parity plot showing nn-EQL's predictions at various stages of training, when compared to the ground truth directivity values. The average error after pruning (Stage 2) (red) and rounding of coefficients during equation read-out (Stage 3) (green) is higher than the error after initial training (Stage 1) (blue).

3. Steering over wide field of view with a spatial refractive index profile made up of a lens and grating

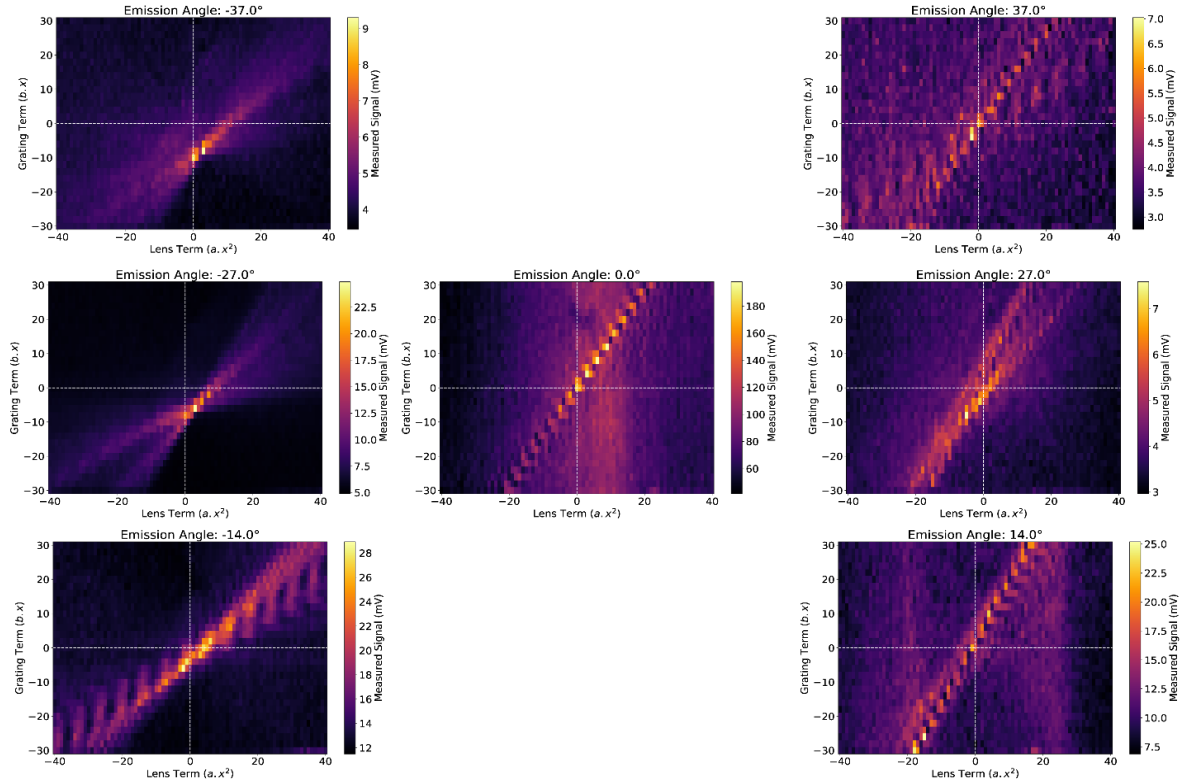


Figure S5: The far-field emission pattern from the metasurface under spatially structured optical pump formed as a combination of a lens ($a.x^2$) and a grating term ($b.x$) from -37° to $+37^\circ$ with the negative angles on the left side and the positive angles on the right side.

References:

1. Bennett, B. & Soref, R. Electro refraction and electro absorption in InP, GaAs, GaSb, InAs, and InSb. *IEEE J Quantum Electron* 23, 2159–2166 (1987)
2. Adachi, S. Model dielectric constants of GaP, GaAs, GaSb, InP, InAs, and InSb. *Phys Rev B* 35, 7454–7463 (1987)
3. Prasankumar, R. P. et al. Ultrafast carrier dynamics in an InAs/InGaAs quantum dots-in-a-well heterostructure. *Optics Express*, Vol. 16, Issue 2, pp. 1165-1173 16, 1165–1173 (2008)
4. Quochi, F. et al. Coulomb and carrier-activation dynamics of resonantly excited InAs/GaAs quantum dots in two-color pump-probe experiments. *Phys Rev B* 67, 235323 (2003).
5. O’Driscoll, I. et al. Electron and hole dynamics of InAs/GaAs quantum dot semiconductor optical amplifiers. *Appl Phys Lett* 91, (2007).
6. Brener, I., Gershoni, D., Ritter, D., Panish, M. B. & Hamm, R. A. Decay times of excitons in lattice-matched InGaAs/InP single quantum wells. *Appl Phys Lett* 58, 965–967 (1991).